The role of porosity evolution and fluid flow in frictional instabilities: A parametric study using a spring-slider dynamic system

AUTHOR(S):

Mitsui, Yuta; Cocco, Massimo

CITATION:

Mitsui, Yuta ...[et al]. The role of porosity evolution and fluid flow in frictional instabilities: A parametric study using a spring-slider dynamic system. Geophysical Research Letters 2010, 37: L23305.

ISSUE DATE:

2010-12

URL:

http://hdl.handle.net/2433/134563

The role of porosity evolution and fluid flow in frictional instabilities: a parametric study using a spring-slider dynamic system

Mitsui Y.,[1] and M. Cocco[2]

Abstract. We have investigated the role of porosity evolution and fluid flow in frictional instabilities by analyzing the response of a single degree of freedom dynamic system. The spring slider is governed by rate- and state-dependent constitutive law. We also account for effective normal stress changes caused by thermal pressurization with constant or variable porosity. Our simulations show that the stress drop during dynamic instabilities depends on constitutive parameters, porosity evolution, fluid flow as well as on the effective fault zone thickness, defined in this study as the ratio between the nominal thickness of the fault zone (w) and the hydraulically activated layer (w_{hy}). Both porosity evolution and fluid flow can avoid the extremely large stress drop values inferred by thermal pressurization models and provide an attempt to reconcile them with seismological observations.

1. Introduction

The role of pore fluid has been intensely discussed in the literature and associated with earthquake nucleation and triggering as well as with frictional instabilities. As an example, thermal pressurization has been proposed as a mechanism to explain low values of effective friction during sliding at high slip rates (*Rice and Cocco* [2007], and references therein). Numerical simulations of dynamic ruptures (*Bizzarri and Cocco* [2006a]) or earthquake recurrent cycles (*Mitsui and Hirahara* [2009]) governed by thermal pressurization yield extremely large stress drop values inconsistent with seismological observations and resulting in a stress drop paradox *Bizzarri and Cocco* [2006b]).

Geological observations suggest that earthquake slip is concentrated in an extremely thin principal slipping surface ([μm] $\sim$ [mm]) embedded in a fault core, whose thickness can range between few [cm] to [m], surrounded by a broader ([10m] $\sim$ [km]) damage zone (*Chester et al.* [1993]; *Rice and Cocco* [2007]). In such a complex fault zone hydraulic (permeability and porosity) and rheological parameters depend on the position within the fault zone. Fault zone porosity is expected to change as a function of slip amount (*Suzuki and Yamashita* [2008]), slip rate, normal stress, grain size of fault gouges etc..., all affecting the frictional instabilities.

The goal of this paper is to jointly interpret the effects of porosity evolution, fluid diffusion and adopted fault zone thickness on the frictional instabilities over earthquake cycles using a single degree of freedom dynamic system (a spring-slider model) (*Rice and Tse* [1986]; *Boatwright and Cocco* [1996]).

[1]Department of Geophysics, Kyoto University, Japan.
[2]Istituto Nazionale di Geofisica e Vulcanologia, Sezione Sismologia e Tettonofisica Rome, Italy.

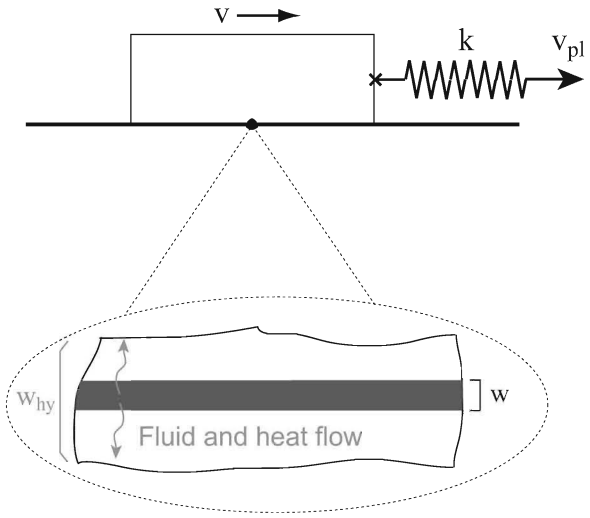

Figure 1. A sketch of the spring-slider system as used in this study. Frictional slip is loaded by a far-field point via spring stiffness k. Frictional heating is generated in a nominal thickness w and w_{hy} is the thickness of the hydraulic activated layer.

2. Methodology

We use a simple spring-slider system to investigate the temporal evolution of shear stress $\tau_f = \mu(\sigma_n - p)$ (that in this study corresponds to frictional resistance) and slip u on an ideal fault (where μ is the sliding friction coefficient, σ_n is the normal stress and p is pore pressure), loaded by a far-field tectonic load via spring stiffness k. The slider is governed by the rate- and state-dependent friction constitutive law (*Ruina* [1983]). Frictional heating increases temperature T that increases fluid pressure p. Our thermal pressurization model can account for porosity ϕ evolution and fluid flow perpendicularly to the fault plane (see Figure 1).

2.1. Constitutive equations for the spring-slider system

Within this mechanical framework, the equation of motion is given by:

$$\frac{P^2}{4\pi^2}\frac{dv}{dt} = (\tau - \tau_f)/k = [\tau_0 + k(v_{pl}t - u) - \mu(\sigma - p)]/k \quad (1)$$

where P is the vibration period, v is the slip rate, t is time, τ_0 is the initial loading stress, v_{pl} is the load point velocity and τ is the loading stress.

The friction coefficient μ depends on the slip rate v and the state variable Θ:

$$\mu = \mu_0 + a \ln\left(\frac{v}{v_0}\right) + b\Theta \tag{2}$$

where μ_0 is a reference frictional coefficient and v_0 is a reference slip rate. a and b are the rate and state constitutive parameters. Θ evolves obeying the slip law modified to include the normal stress changes as proposed by *Linker and Dieterich* [1992]:

$$\frac{d\Theta}{dt} = \frac{-v}{L}(\Theta - \Theta_{ss}) - \frac{\xi_{LD}}{b(\sigma_{eff})}\frac{d\sigma_{eff}}{dt} \tag{3}$$

where L is the characteristic length scale parameter of the state evolution, $\sigma_{eff} = (\sigma - p)$ is the effective normal stress and ξ_{LD} is a lab-derived parameter (its value ranges between $0.2 - 0.3$). The steady-state value of the state variable Θ_{ss} is given by $\ln(v_0/v)$. We follow the simulation strategy proposed by *Boatwright and Cocco* [1996], details are described in Appendix A.

2.2. Constitutive equations for pore pressure evolution

As written in Chapter III, the pore pressure changes in thermo-poroelastic media can be described as

$$\frac{dp}{dt} = \Lambda\frac{dT}{dt} - \frac{1}{(\beta_f + \beta)\phi}\frac{d\phi}{dt}\bigg|_{pl} + \varpi\nabla^2 p \tag{4}$$

where Λ is $(\alpha_f - \alpha)/(\beta_f + \beta)$, α_f and α are the thermal expansivity of pore fluid and solid, respectively; β_f and β are pressure expansivity of pore fluid and solid, respectively; ϕ is the porosity, and ϖ is the fluid diffusivity corresponding to $\kappa/[\nu\phi(\beta_f + \beta)]$, where κ is the permeability and ν is the viscosity of the pore fluid.

The first right-hand term of Equation (4) represents frictional heating and heat flow. We assume the shear strain rate is approximated by v/w, where v is the macroscopic slip rate (*Cocco and Tinti* [2008]) and w is the thickness of the fault zone where strain is localized (see Figure 1). Because heat source scales with slip rate, we can consider w as the zone where heat is generated (*Fialko* [2004]); hereinafter we refer to w with such a meaning. Thus that term can be written as:

$$\frac{dT}{dt} = \frac{1}{\rho c}\left(\frac{\tau_f v}{w}\right) + \chi\nabla^2 T \tag{5}$$

where $\chi = \lambda/(\rho c)$ is the temperature diffusivity, where λ is thermal diffusivity and ρc is the heat capacity per unit volume.

Substituting equation (5) into equation (4), we obtain

$$\frac{dp}{dt} = A\frac{\tau_f v}{w} - \frac{1}{(\beta_f + \beta)\phi}\frac{d\phi}{dt}\bigg|_{pl} + \varpi\nabla^2 p + \Lambda\chi\nabla^2 T \tag{6}$$

where A corresponds to $\Lambda/(\rho c)$. This equation is identical to equation (A2) in *Bizzarri and Cocco* [2006b]. If we solve equation (6) simultaneously with (1), we have to adopt the discrete approximation (e.g., *Segall and Rice* [1995]) for the diffusion terms. To avoid this approximation, we use the closed-form solution derived by *Bizzarri and Cocco* [2006b]

$$p(t) = p_0 + \frac{A}{w}\int_0^t dt' \left[-\frac{\chi}{\varpi - \chi}\mathrm{erf}\left(\frac{w}{4\sqrt{\chi(t-t')}}\right) + \frac{\varpi}{\varpi - \chi}\mathrm{erf}\left(\frac{w}{4\sqrt{\varpi(t-t')}}\right)\right] \cdot\left(\mu(\sigma - p)v - \frac{w}{A(\beta + \beta_f)\phi}\frac{d\phi}{dt'}\right)\bigg|_{t'} \tag{7}$$

where p_0 is the initial value of the pore pressure p. In addition, we will introduce a thickness of the hydraulically activated layer w_{hy}, defined as $w_{hy} = 2\sqrt{\varpi P}$ (see *Rudnicki* [1986] and references therein), to normalize the adopted nominal fault zone thickness w. In this definition we use the period P as a measure of slip duration (*Rice and Tse* [1986]).

In order to account for porosity changes in (7), we adopt the porosity evolution equation proposed by *Segall and Rice* [1995] and *Sleep* [1995]:

$$\frac{d\phi}{dt} = -\epsilon\frac{d\Theta}{dt} \tag{8}$$

where ϵ is a lab-derived parameter (namely a dilatancy coefficient). *Segall and Rice* [1995] proposed $\epsilon = 1.7 \times 10^{-4}$ and more recently *Samuelson et al.* [2009] found ϵ ranges from 4.7×10^{-5} to 3.0×10^{-4}. In our manuscript, we refer to $\epsilon = 1.7 \times 10^{-4}$ as the "lab value". The constitutive formulation adopted in this study associates porosity changes with state variable changes, inferred from laboratory experiments on fault gouge behavior (see *Marone et al.* [1990]). This means that the zone affected by porosity changes is the fault thickness w.

3. Results

In this section, we present and discuss the results of several numerical computations. The physical parameters that we have fixed in all calculations are listed in Table 1. We have investigated five distinct configurations for our simulations, each of which is identified by the following parameterization:

1. $a = 0.007$, $b = 0.016$, $L = 0.01$[m], $k = 0.8[(\sigma - p_0)(b - a)]/L$, $P = 5$[s], $\xi_{LD} = 0.0$
2. $a = 0.007$, $b = 0.016$, $L = 0.01$[m], $k = 0.8[(\sigma - p_0)(b - a)]/L$, $P = 50$[s], $\xi_{LD} = 0.0$
3. $a = 0.007$, $b = 0.016$, $L = 0.01$[m], $k = 0.8[(\sigma - p_0)(b - a)]/L$, $P = 50$[s], $\xi_{LD} = 0.3$

Table 1. Common parameters in this study.

Property	Symbol	Value	Units
Load point velocity	v_{pl}	0.045	m/yr
Reference slip rate	v_0	0.0375	m/yr
Cut-off slip rate	v_{dy}	0.1	mm/s
Normal stress	σ	130	MPa
Reference pore pressure	p_0	100	MPa
Frictional coefficient	μ_0	0.56	
Reference loading stress	τ_0	16.8	MPa
Compressibility	$\beta_f + \beta$	1.0×10^{-9}	/Pa
Thermal expansion coefficient	$\alpha_f - \alpha$	1.5×10^{-3}	/K
Fluid viscosity	ν	1.0×10^{-4}	Pa·s
Thermal conductivity	λ	3.0	W/m·K
Heat capacity per unit weight	ρc	3.0×10^{6}	J/m^3·K
Reference porosity	ϕ_0	0.025	

4. $a = 0.007$, $b = 0.012$, $L = 0.0005$[m], $k = 0.8[(\sigma - p_0)(b-a)]/L$, $P = 5$[s], $\xi_{LD} = 0.0$

5. $a = 0.007$, $b = 0.012$, $L = 0.0005$[m], $k = 0.4[(\sigma - p_0)(b-a)]/L$, $P = 5$[s], $\xi_{LD} = 0.0$

We refer to each parameterization as a distinct model (Model i, $i = 1, 5$). In models 1, 2 and 3, we have chosen the same values for a, b, L (the constitutive parameters of the rate- and state-dependent friction law) as well as the same value for the stiffness k. Here we introduce the critical stiffness $k_c = (b-a)(\sigma - p_0)/L$ (we will discuss more in detail this parameter in Appendix E. Models 1, 2 and 3 have the same ratio k/k_c, but they differ for the values of P (characteristic period of dynamic motion) and ξ_{LD} (parameter for the effect of normal stress on the state evolution). Models 4 and 5 have the same set of a, b, L and k_c (differing from models 1-3), but a different stiffness. Therefore, models 1, 2 and 3 have been identified to investigate the effects of P and ξ_{LD}, while models 4 and 5 have been designed to study the effect of the stiffness. Their comparison allows the understanding of the role of the frictional parameters as well as of the ratio k/k_c.

For each of these models we have performed simulations by varying the permeability κ and then hydraulic diffusivity ϖ, the fault zone thickness w, the parameter ϵ of porosity evolution law. For the latter parameter, we have tried three values: $\epsilon = 0$ (only thermal pressurization), 1.7×10^{-4} (lab-derived value) and 1.7×10^{-5} (smaller value). Because we vary the diffusivity, for the same w, different simulations can have different thicknesses of the hydraulically activated layer ($w_{hy} = 2\sqrt{\varpi P}$) and therefore different ratios between w/w_{hy}. As a result, we obtain various values of static stress drop S_s and the instability recurrence time R_i, where S_s is defined as a difference between maximum shear stress and the stress at the recovery point of quasi-static equilibrium after slip instability.

The adopted constitutive parameters and the inferred physical quantities for each configuration are listed in Tables 2-6. ΔT_{max} is the maximum increase of temperature. S_s^0 and R_i^0 are S_s and R_i in the cases with constant pore pressure (that is, a slider solely governed by rate & state friction).

Figure 2 shows the normalized shear stress, $(\tau_f - \tau_0)/[a(\sigma - p_0)]$, as a function of slip (a) and slip rate (b) computed for model 1 for a slider governed by rate- and state-dependent friction (R & S, black curves), by thermal pressurization (TP, green curves) and by thermal pressurization with porosity evolution (TPPE, red curves). This figure clearly shows that the slider solely governed by R & S displays a clear dynamic weakening (traction drops with increasing slip) followed by slip at the steady-state. In contrast, the slider governed by thermal pressurization shows a continuous weakening (stress decrease) for the whole duration and a larger stress drop. It is worthy of noting that the inclusion of porosity evolution can counterbalance the effect of frictional heating and fluid flow resulting in a stress drop similar to that of the slider solely governed by R & S. Moreover, the phase diagram shown in Figure 2b illustrates that the shear stress during the slip acceleration and the peak slip velocity are nearly the same for the three constitutive formulations, but TP produces a larger stress drop consistent with *Mitsui and Hirahara* [2009] and *Bizzarri and Cocco* [2006b]. The porosity and temperature changes associated with the simulations shown in Figure 2 are discussed in Appendix B and C.

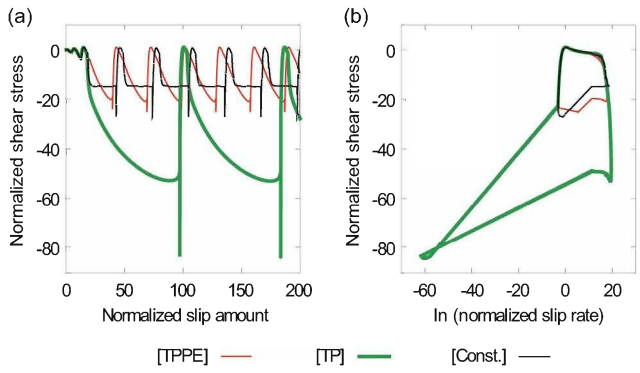

Figure 2. Shear stress evolution computed for Model 1 (see text and Appendix) with $\varpi = 0.002$ [m^2/s] and $w = 0.08$ [m]. Normalized shear stress $(\tau_f - \tau_0)/[a(\sigma - p_0)]$ is plotted as a function of normalized slip u/L (a) and slip rate $\ln(v/v_0)$ (b). Black solid curves display the stress evolution for a slider solely obeying to $R\&S$ friction. Green and red curves show the results for thermal pressurization with constant and with variable porosity, respectively. In these simulations, $w = 0.08$ [m] and $\epsilon = 1.7 \times 10^{-4}$. All of the traces in panel (b) rotate clockwise.

We have performed different simulations accounting for different characteristic periods, frictional properties and stiffness of the slider. Our simulations show that the stress drop depends on porosity evolution, hydraulic diffusivity and nominal thickness w. In this study, we try to jointly interpret the effects caused by all these parameters over the seismic cycle.

4. Discussion

In order to better understand the effectiveness of porosity evolution to counterbalance thermal pressurization, we have compared the static stress drop calculated from simulations performed taking into account TP only with those accounting for TPPE. Moreover, to emphasize the role of hydraulic diffusivity and w, we have investigated the scaling of the ratio between these static stress drop estimates with the ratio between w and the thickness of the hydraulically activated layer w_{hy}.

The results of these calculations are summarized in Figure 3, in which panels (a) & (c) and (b) & (d) refer to two different estimates of the dilatancy coefficient ϵ (1.7×10^{-4} and 1.7×10^{-5}, respectively). This figure shows that for $w/w_{hy} \ll 1$, the static stress drop associated with TPPE is of the same order as that associated with TP only. This can be either due to a negligible contribution of porosity evolution, unable to counterbalance thermal pressurization because of intense frictional heating (thin slipping zone), or small values in stress drop for both TP and TPPE because of rapid fluid flow (e.g., drained conditions). In contrast, when $w/w_{hy} \to 1$ (see Appendix D) and ϵ is large (lab value), the static stress drop ratio is extremely small because porosity evolution is able to compensate for TP (see panels (a) and (c)) and stress drop estimates for TPPE are much smaller than those for TP only. Panels (b) and (d) in Figure 3 show that decreasing the value of the ϵ parameter reduces the role of porosity evolution on the stress drop ratio.

The dashed lines in Figure 3 display the parametric fit through an exponential function $y = \exp(-\zeta(w/w_{hy}))$. The different values of the ζ exponent in panels (a) and (c) and (b) and (d) (4.5 & 15 and 0.45 & 1.5, respectively) indicate that $\zeta \propto \epsilon$. Moreover, panels (c) and (d) of Figure 3 depict the result for models 4 and 5, which are characterized by smaller values of L and larger critical stiffness $k_{c0} = (\sigma - p_0)(b-a)/L$ (they differ for the value of the ratio k/k_{c0}). In Appendix E, we discuss that in our simulations k_{c0} does not substantially differ from the more appropriate critical stiffness k_c proposed by *Segall and Rice* [1995] for a fluid infiltrated fault with variable porosity. The results

of these simulations demonstrate that the effectiveness of porosity evolution to counterbalance thermal pressurization also depends on the critical stiffness (k_c) of the dynamic system (in agreement with *Segall and Rice* [1995]). The ζ parameter for the best fitting exponential curve in panels (c) and (d) are larger than those of panels (a) and (b) (see the values in each panel), confirming the dependence on the ϵ parameter and suggesting $\zeta \propto \sqrt{k_c}$ (more unstable systems lead to more effective counteraction of porosity evolution).

5. Conclusion

We have used a simple degree of freedom dynamic system in order to perform a parametric study and quantify the impact of porosity changes within the fault zone. This assumption allows us to simulate the seismic cycle and to assess this effect during the different phases of the cycle, not limiting our analysis to the dynamic instability. Our results demonstrate that porosity evolution, fluid flow and the nominal value of fault zone thickness control the stress drop during dynamic instabilities. Our results show that porosity evolution can compensate for the effects of thermal pressurization by reducing pore pressure. This case yields in the undrained condition limit ($w/w_{hy} \to 1$). By contrast, in the limit $w/w_{hy} \to 0$, porosity evolution does not act on the stress drop. In case that fluid flow dominates (drained conditions), both the effects of porosity evolution and frictional heating becomes not effective. Moreover, in agreement with previous studies (e.g., *Bizzarri and Cocco* [2006b]; *Suzuki and Yamashita* [2008]; *Mitsui and Hirahara* [2009]), small values of the nominal fault zone thickness w intensify the effect of shear heating. To further corroborate our results, we have performed additional tests with different w but keeping w/w_{hy} constant (see Appendix F).

In our simulations, we allowed porosity to change, keeping permeability constant. This configuration is representative of faults in which porosity evolution does not change pore connectivity within the fault zone. An alternative approach to link porosity evolution with permeability changes is presently limited by the lack of appropriate analytical relationships between these two parameters. This represents a challenge to tackle in the near future for both laboratory experiments and numerical modeling.

Several studies in the literature suggest that permeability within the fault core is smaller than permeability in the damage zone, which implies that the border between fault core and damage zone is an impermeable layer. This means that the fault core thickness may represent an upper bound for the hydraulically activated layer (w_{hy}). Because w (the zone where heat is generated) should range between the thickness of the principal shear zone and the fault core, such a configuration would limit the variability of the ratio w/w_{hy} to relatively high values (that is, ~ 1), thus allowing porosity evolution to play a role in the breakdown process and to provide a solution to the stress drop paradox raised by thermal pressurization models.

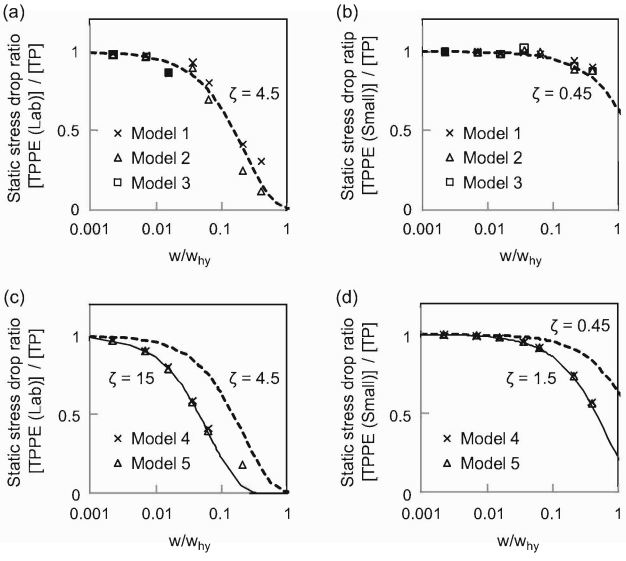

Figure 3. The ratio between the static stress drops inferred from simulations with thermal pressurization and porosity evolution (TPPE) and those with thermal pressurization and constant porosity (TP) is plotted as a function of the effective fault thickness given by the ratio w/w_{hy}. The results in panels (a) and (b) are inferred from models 1, 2 and 3, while those in panels (c) and (d) are obtained from models 4 and 5 (see Appendix). Panels (a) and (c) show the outcomes of simulations performed using a laboratory value for $\epsilon = 1.7 \times 10^{-4}$, while panels (b) and (d) display those obtained by setting $\epsilon = 1.7 \times 10^{-5}$. Dashed and solid curves represent the fits obtained through an exponential function $y = \exp(-\zeta(w/w_{hy}))$, the inferred value of the ζ parameter is indicated in each panel.

A. Numerical Strategy

In this study we follow the simulation strategy proposed by *Boatwright and Cocco* [1996]. We solve the equation of motion for a spring slider system governed by rate- and state-dependent friction law including inertia and accounting for thermo-poro-elastic processes. The set of equations that we simultaneously solve is the following:

$$\frac{P^2}{4\pi^2}\frac{dv}{dt} = (\tau - \tau_f)/k = [\tau_0 + k(v_{pl}t - u) - \mu(\sigma - p)]/k \quad (9)$$

$$\mu = \mu_0 + a\ln\left(\frac{v}{v_0}\right) + b\Theta \quad (10)$$

$$\frac{d\Theta}{dt} = \frac{-v}{L}(\Theta - \Theta_{ss}) - \frac{\xi_{LD}}{b(\sigma_{eff})}\frac{d\sigma_{eff}}{dt} \quad (11)$$

$$\frac{d\phi}{dt} = -\epsilon\frac{d\Theta}{dt} \quad (12)$$

$$p(t) = p_0 + \frac{A}{w}\int_0^t dt'\left[-\frac{\chi}{\varpi - \chi}\mathrm{erf}\left(\frac{w}{4\sqrt{\chi(t-t')}}\right) + \frac{\varpi}{\varpi - \chi}\mathrm{erf}\left(\frac{w}{4\sqrt{\varpi(t-t')}}\right)\right] \cdot\left(\mu(\sigma - p)v - \frac{w}{A(\beta + \beta_f)\phi}\frac{d\phi}{dt'}\right)\Bigg|_{t'} \quad (13)$$

We include an upper threshold for the slip rate v referring to a rock experimental study *Weeks* [1993]: During dynamic instabilities (identified by $v \geq v_{dy}$, where v_{dy} must be less than $2\pi L/P$ and is fixed to 0.1 [mm/s]), the steady-state value of state variable Θ_{ss} is assumed to be constant and its value is equal to $\ln(v_0/v_{dy})$. Moreover, the direct dependence of slip rate in Equation (10) is frozen and given by $a\ln(v_{dy}/v_0)$.

On the contrary, during the quasi-static phase ($v < v_{dy}$), we neglect inertia in Equation (9). Then, substituting Equation (10) into Equation (9), we obtain

$$v = v_0 \exp\left(\left[\frac{\tau_0 + k(v_{pl}t - u)}{\sigma - p} - \mu_0 - b\Theta\right]/a\right) \quad (14)$$

When $v = v_{dy}$ just after the dynamic period, we must impose that $\tau_0 + k(v_{pl}t - u) = \mu(\sigma - p)$ to recover the quasi-static condition.

In the numerical calculations, we assume steady-state values as initial conditions: $v = v_{pl}$, $\Theta = \ln(v_0/v_{pl})$, $\phi = \phi_0 + \epsilon \ln(v_{pl}/v_0)$, $p = p_0$ and $\tau = \tau_0 + (a-b)(\sigma - p)\ln(v_{pl}/v_0)$. To solve the governing equations presented above, we first use the RK45 algorithm (*Press et al.* [1992]) with adaptive step-size control to obtain the evolution of τ, ϕ, Θ and v. During the dynamic phase we solve equations (Equations (9)-(12)), and during the quasi-static phase we only solve $d\phi/dt$ and $d\Theta/dt$ to determine v (Equations (11), (12) and (14)), and get a tentative value of p by Equation (13). Then, using it, all of the variables are re-calculated following a second-order Runge-Kutta method. When the slip rate v does not exceed v_{pl}, the memory of the shear heating term is not stored as in *Mitsui and Hirahara* [2009].

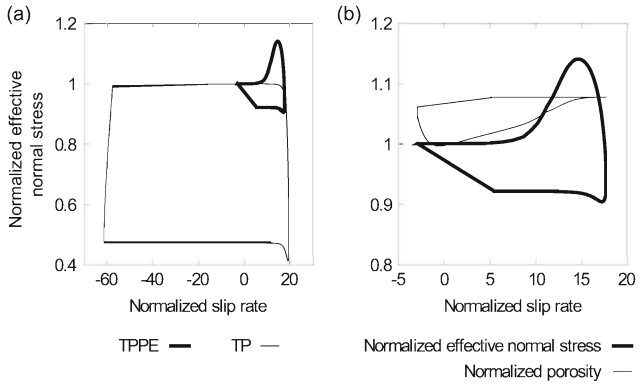

Figure 4. Normalized normal stress $(\sigma - p)/(\sigma - p_0)$ evolution as a function of normalized slip rate $\ln(v/v_0)$ for the same simulations shown in Figure 2 ($\varpi = 0.002$ [m^2/s], $w = 0.08$ [m] and $\epsilon = 0$ or 1.7×10^{-4}). Panel (a) shows the comparison between two simulations in which the slider is governed by thermal pressurization with constant or variable porosity. For the latter case, panel (b) displays the evolutions of normalized effective normal stress and normalized porosity (ϕ/ϕ_0). The traces of effective normal stress rotate clockwise and that of porosity does counter-clockwise.

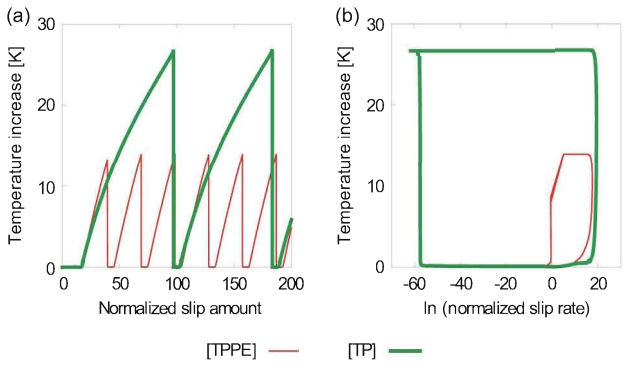

Figure 5. Temperature evolution computed for the same simulations shown in Figure 2 ($\varpi = 0.002$ [m^2/s], $w = 0.08$ [m] and $\epsilon = 0$ or 1.7×10^{-4}). Increase of temperature ΔT is plotted as a function of normalized slip u/L (a) and slip rate $\ln(v/v_0)$ (b). Green and red curves show the results for thermal pressurization with constant and with variable porosity, respectively. All of the traces in panel (b) rotate clockwise.

B. Porosity changes

Figure 4 summarizes the difference between TP (thermal pressurization with constant porosity) and TPPE (thermal pressurization with porosity changes) models. Thermal pressurization with constant porosity involves a large variation of the effective normal stress (panel a) if compared to that inferred for porosity evolution. For this latter case, panel b allows the comparison between effective normal stress and porosity evolution.

This figure demonstrates that porosity increase (that is, diffusivity decrease) can explain the inferred effective normal stress evolution and the static stress drop reduction. These results are consistent with those of (*Segall and Rice* [1995]), but extend them to an interesting and original comparison with thermal pressurization models.

C. Temperature changes

Figure 5 shows an example of the temperature evolutions in TP (thermal pressurization with constant porosity) and TPPE (thermal pressurization with porosity changes) models. In both models, temperature suddenly increases with slip acceleration and decreases by heat diffusion after slip deceleration. The maximum increase in temperature tends to be restrained by porosity evolution. In our calculations, temperature does not reach high values to melt fault gouge as listed in Tables 2-6. Of course occurrence of melting would completely change the fault frictional behavior (see *Nielsen et al.* [2008])); discussing this issue is beyond the scope of this paper.

D. Other type of normalization for fault zone thickness

The adimentional thickness w/w_{hy} that we have adopted in Figure 3 does not allow us to consider fully undrained conditions ($w_{hy} = 0$, leading to $w/w_{hy} \to \infty$). However, this limitation does not affect the conclusions obtained in this study. An alternative solution to avoid such problem might be to adoption of a different normalization for w: $w/(w_{hy} + w)$. In this case, the undrained limit can be represented as $w/(w_{hy} + w) \to 1$. In order to confirm that our conclusions are not affected by this choice, we plot in Figure 6 the same stress drop ratios shown in Figure 3 as a function $w/(w_{hy} + w)$.

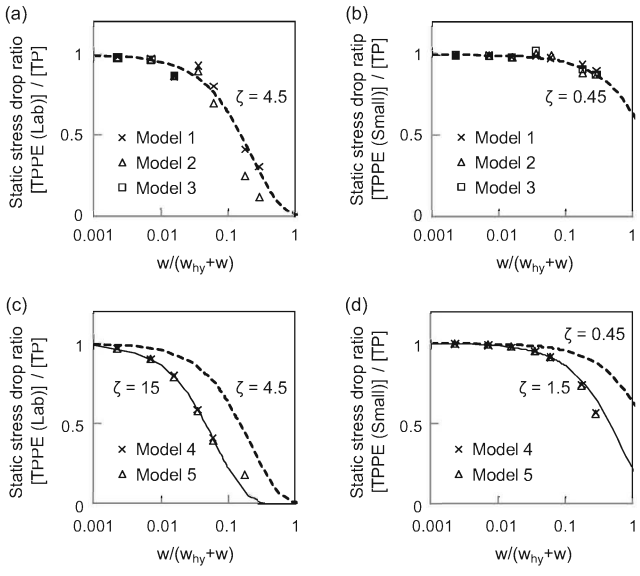

Figure 6. The same calculation results in Figure 3 but replotted versus $w/(w_{hy} + w)$.

E. Critical stiffness

Our results imply that the stress drop ratio between TP and TPPE models has an exponential-type dependence $y = \exp(-\zeta(w/w_{hy}))$, and ζ would be proportional to ϵ and k_c. Here, we adopt the critical stiffness is given by $k_c = (b-a)(\sigma - p_0)/L$ (hereinafter called k_{c0}). This is originally derived by *Ruina* [1983] using linear stability analysis with assumptions of the quasi-static regime and constant pore pressure. However, strictly speaking, its use is not appropriate for our models with variable pore pressure (see *Segall and Rice* [1995]).

Segall and Rice [1995] obtained more complicated representation of the critical stiffness (we call it k_{cSR}), when pore pressure varies with their porosity evolution law. k_{cSR} has a shape of $k_{c0} - F(\varpi)\epsilon\mu_{0p}/(\phi_0(\beta_f+\beta)L)$, where $\mu_{0p} = \mu_0 + (a-b)\ln(v_{pl}/v_0)$ and F is a function of the hydraulic diffusivity and frictional parameters. However, their original formulation contains a fixed characteristic diffusion length that we do not assume in our formulation. As a trial of matter, we substitute w_{hy} in our model into their constant diffusion length. Then "c^*" in their model is changed into $\varpi/w_{hy}^2 = 1/(4P)$. By adopting this strategy, we have verified that $k_{cSR} \simeq k_{c0}$ in all cases considered in this study. That is, we can adopt $k_c \simeq k_{c0}$ to account for the dependence of stress drop ratio on ζ.

F. Same w/w_{hy} but different w and w_{hy}

In order to check the dependence on w/w_{hy}, we have performed several further numerical experiments (model 4+). In model 4+, we assume the same set of a, b, L, k, P and ξ_{LD} of model 4, but different w and w_{hy} to have the same w/w_{hy} in each simulation. The results are listed in Table 7.

Figure 7 illustrates the ratio between the static drops with thermal pressurization and porosity evolution (TPPE) and those with thermal pressurization and constant porosity (TP) as a function of the effective fault thickness given by the ratio w/w_{hy}. We show the results of simulations obtained by using a laboratory value for $\epsilon = 1.7 \times 10^{-4}$, which corresponds to the results in Figure 3(c). This test allows us to confirm that with different w, but the same w/w_{hy}, our results do not change. This corroborates the inferred dependence on w/w_{hy}.

Acknowledgments. We thank Giulio Di Toro, Stefan Nielsen, Yehuda Ben-Zion, Kazuro Hirahara and Andre Niemeijer for helpful discussions and criticisms on this study. We benefit from detailed and effective comments by Maria Elina Belardinelli and Takehito Suzuki, who reviewed this manuscript.

References

Bizzarri, A., and M. Cocco (2006a), A thermal pressurization model for the spontaneous dynamic rupture propagation on a three-dimensional fault: 1. Methodological approach, *J. Geophys. Res.*, *111*(B5), doi:10.1029/2005JB003862.

Bizzarri, A., and M. Cocco (2006b), A thermal pressurization model for the spontaneous dynamic rupture propagation on a three-dimensional fault: 2. Traction evolution and dynamic parameters, *J. Geophys. Res.*, *111*(B5), doi:10.1029/2005JB003864.

Boatwright, J., and M. Cocco (1996), Frictional constraints on crustal faulting, *J. Geophys. Res.*, *101*(B6), 13,895–13,909, doi:10.1029/96JB00405.

Chester, F. M., J. P. Evans, and R. L. Biegel (1993), Internal Structure and Weakening Mechanisms of the San Andreas Fault, *J. Geophys. Res.*, *98*(B1), 771–786, doi:10.1029/92JB01866.

Cocco, M., and E. Tinti (2008), Scale dependence in the dynamics of earthquake propagation: Evidence from seismological and geological observations, *Earth Planet. Sci. Lett.*, *273*(1-2), 123–131, doi:10.1016/j.epsl.2008.06.025.

Fialko, Y. (2004), Temperature fields generated by the elastodynamic propagation of shear cracks in the Earth, *J. Geophys. Res.*, *109*(B1), doi:10.1029/2003JB002497.

Linker, M. F., and J. H. Dieterich (1992), Effects of Variable Normal Stress on Rock Friction: Observations and Constitutive Equations, *J. Geophys. Res.*, *97*(B4), 4923–4940, doi:10.1029/92JB00017.

Marone, C., C. B. Raleigh, and C. H. Scholz (1990), Frictional Behavior and Constitutive Modeling of Simulated Fault Gouge, *J. Geophys. Res.*, *95*(B5), 7007–7025, doi:10.1029/JB095iB05p07007.

Mitsui, Y., and K. Hirahara (2009), Coseismic thermal pressurization can notably prolong earthquake recurrence intervals on weak rate and state friction faults: Numerical experiments using different constitutive equations, *J. Geophys. Res.*, *114*(B9), doi:10.1029/2008JB006220.

Nielsen, S., G. Di Toro, T. Hirose, and T. Shimamoto (2008), Frictional melt and seismic slip, *J. Geophys. Res.*, *113*(B1), doi:10.1029/2007JB005122.

Press, W. H., B. P. Teukolsky, and W. T. Vetterling (1992), *Numerical Recipes*, 2nd ed., Cambridge University Press, New York.

Rice, J. R., and M. Cocco (2007), Seismic Fault Rheology and Earthquake Dynamics, in *Tectonic Faults: Agents of Change on a Dynamic Earth*, edited by M. R. Handy, G. Hirth, and N. Hovius, chap. 5, pp. 99–137, (Dahlem Workshop 95 Berlin, January 2005, On The Dynamics Of Fault Zones), The MIT Press.

Rice, J. R., and S. T. Tse (1986), Dynamic Motion of a Single Degree of Freedom System Following a Rate and State Dependent Friction Law, *J. Geophys. Res.*, *91*(B1), 521–530, doi:10.1029/JB091iB01p00521.

Rudnicki, J. W. (1986), Slip on an impermeable fault in fluid-saturated rock mass, in *Earthquake source mechanics*, *AGU Geophysical Monograph 37*, vol. 6, edited by S. Das, J. Boatwright, and C. H. Scholz, pp. 81–89.

Ruina, A. (1983), Slip Instability and State Variable Friction Laws, *J. Geophys. Res.*, *88*(B12), 10,359–10,370, doi:10.1029/JB088iB12p10359.

Samuelson, J., D. Elsworth, and C. Marone (2009), Shear-induced dilatancy of fluid-saturated faults: Experiment and theory, *J. Geophys. Res.*, *114*(B12), doi:10.1029/2008JB006273.

Segall, P., and J. R. Rice (1995), Dilatancy, compaction, and slip instability of a fluid-infiltrated fault, *J. Geophys. Res.*, *100*(B11), 22,155, doi:10.1029/95JB02403.

Sleep, N. H. (1995), Ductile creep, compaction, and rate and state dependent friction within major fault zones, *J. Geophys. Res.*, *100*(B7), 13,065, doi:10.1029/94JB03340.

Suzuki, T., and T. Yamashita (2008), Nonlinear effects of temperature, fluid pressure, and inelastic porosity on dynamic fault slip and fault tip propagation: Emergence of slip strengthening and pulse-like fault slip, *J. Geophys. Res.*, *113*(B7), doi:10.1029/2008JB005581.

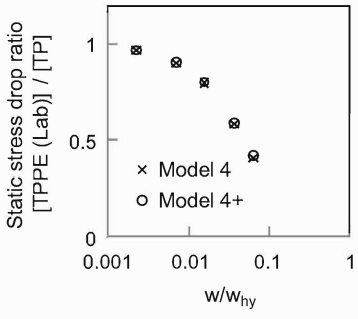

Figure 7. The ratio between the static stress drops inferred from simulations with thermal pressurization and porosity evolution (TPPE) and those with thermal pressurization and constant porosity (TP) is plotted as a function of the effective fault thickness given by the ratio w/w_{hy}. The results are obtained from models 4 and 4+. The simulations performed using a laboratory value for $\epsilon = 1.7 \times 10^{-4}$ (Lab value).

Weeks, J. D. (1993), Constitutive Laws for High-Velocity Frictional Sliding and Their Influence on Stress Drop During Unstable Slip, *J. Geophys. Res.*, *98*(B10), 17,637–17,648, doi: 10.1029/93JB00356.

Table 2. Results of Model 1. S_s^0 and R_i^0 are S_s and R_i in the cases with constant pore pressure. S_s^0 is 27.9 and R_i^0 is 6.9 [yr].

κ [m^2]	ϖ [m^2/s]	w [m]	$w/w_{\rm hy}$	ϵ	S_s	S_s/S_s^0	R_i [yr]	R_i/R_i^0	ΔT_{max} [K]
1.0×10^{-17}	0.004	0.002	0.007	(Zero)	82.6	2.97	18.7	2.71	528.5
1.0×10^{-17}	0.004	0.002	0.007	(Lab value)	80.9	2.90	18.4	2.67	527
1.0×10^{-17}	0.004	0.002	0.007	(Small value)	82.5	2.96	18.7	2.71	528.3
1.0×10^{-16}	0.04	0.002	0.002	(Zero)	41.1	1.47	9.8	1.42	414.4
1.0×10^{-16}	0.04	0.002	0.002	(Lab value)	40.3	1.45	9.6	1.39	408.4
1.0×10^{-16}	0.04	0.002	0.002	(Small value)	41.0	1.47	9.7	1.41	413.8
1.0×10^{-17}	0.004	0.018	0.06	(Zero)	80.6	2.89	18.3	2.65	118.1
1.0×10^{-17}	0.004	0.018	0.06	(Lab value)	64.9	2.33	14.9	2.16	113.6
1.0×10^{-17}	0.004	0.018	0.06	(Small value)	79.0	2.84	18.0	2.61	118.1
6.0×10^{-18}	0.0024	0.008	0.04	(Zero)	95.1	3.41	21.3	3.09	245.1
6.0×10^{-18}	0.0024	0.008	0.04	(Lab value)	88.5	3.18	20.0	2.90	250.9
6.0×10^{-18}	0.0024	0.008	0.04	(Small value)	94.4	3.39	21.2	3.07	246.0
5.0×10^{-15}	2	0.1	0.02	(Zero)	29.3	1.05	7.2	1.04	12.4
5.0×10^{-15}	2	0.1	0.02	(Lab value)	25.4	0.91	6.4	0.93	11.0
5.0×10^{-15}	2	0.1	0.02	(Small value)	28.9	1.04	7.1	1.03	12.3
1.0×10^{-17}	0.004	0.06	0.21	(Zero)	72.6	2.60	16.6	2.40	34.9
1.0×10^{-17}	0.004	0.06	0.21	(Lab value)	30.0	1.08	7.4	1.07	20.8
1.0×10^{-17}	0.004	0.06	0.21	(Small value)	68.2	2.45	15.6	2.26	34.9
5.0×10^{-18}	0.002	0.08	0.4	(Zero)	84.6	3.03	19.0	2.75	26.8
5.0×10^{-18}	0.002	0.08	0.4	(Lab value)	26.2	0.94	6.5	0.94	13.9
5.0×10^{-18}	0.002	0.08	0.4	(Small value)	76.2	2.73	17.4	2.52	26.8

Table 3. Results of Model 2. S_s^0 is 27.5 and R_i^0 is 6.8 [yr].

κ [m^2]	ϖ [m^2/s]	w [m]	$w/w_{\rm hy}$	ϵ	S_s	S_s/S_s^0	R_i [yr]	R_i/R_i^0	ΔT_{max} [K]
1.0×10^{-18}	0.0004	0.002	0.007	(Zero)	67.6	2.46	15.5	2.28	173.9
1.0×10^{-18}	0.0004	0.002	0.007	(Lab value)	65.2	2.38	15.0	2.21	170.4
1.0×10^{-18}	0.0004	0.002	0.007	(Small value)	67.4	2.45	15.5	2.28	173.6
1.0×10^{-17}	0.004	0.002	0.002	(Zero)	36.1	1.32	8.7	1.28	120.7
1.0×10^{-17}	0.004	0.002	0.002	(Lab value)	35.5	1.29	8.6	1.26	118.2
1.0×10^{-17}	0.004	0.002	0.002	(Small value)	36.1	1.31	8.7	1.28	120.5
1.0×10^{-18}	0.0004	0.018	0.06	(Zero)	68.8	2.51	15.8	2.32	100.8
1.0×10^{-18}	0.0004	0.018	0.06	(Lab value)	47.9	1.75	11.3	1.66	84.3
1.0×10^{-18}	0.0004	0.018	0.06	(Small value)	68.7	2.50	15.8	2.32	102.4
6.0×10^{-19}	0.00024	0.008	0.04	(Zero)	83.1	3.03	18.9	2.78	148.8
6.0×10^{-19}	0.00024	0.008	0.04	(Lab value)	74.4	2.71	17.0	2.50	146.1
6.0×10^{-19}	0.00024	0.008	0.04	(Small value)	83.9	3.05	19.0	2.79	151.0
5.0×10^{-16}	0.2	0.1	0.02	(Zero)	28.5	1.04	7.1	1.04	11.7
5.0×10^{-16}	0.2	0.1	0.02	(Lab value)	24.7	0.90	6.3	0.93	10.2
5.0×10^{-16}	0.2	0.1	0.02	(Small value)	28.1	1.02	7.0	1.03	11.5
1.0×10^{-18}	0.0004	0.06	0.21	(Zero)	66.7	2.43	15.3	2.25	34.2
1.0×10^{-18}	0.0004	0.06	0.21	(Lab value)	12.9	0.47	4.1	0.60	8.0
1.0×10^{-18}	0.0004	0.06	0.21	(Small value)	59.5	2.17	13.8	2.03	32.7
5.0×10^{-19}	0.0002	0.08	0.4	(Zero)	80.6	2.94	18.3	2.69	26.7
5.0×10^{-19}	0.0002	0.08	0.4	(Lab value)	9.5	0.35	4.0	0.59	5.0
5.0×10^{-19}	0.0002	0.08	0.4	(Small value)	71.2	2.59	16.3	2.40	26.5

Table 4. Results of Model 3. S_s^0 is 27.5 and R_i^0 is 6.8 [yr].

κ [m^2]	ϖ [m^2/s]	w [m]	$w/w_{\rm hy}$	ϵ	S_s	S_s/S_s^0	R_i [yr]	R_i/R_i^0	ΔT_{max} [K]
1.0×10^{-18}	0.0004	0.002	0.007	(Zero)	70.9	2.58	16.3	2.40	185.0
1.0×10^{-18}	0.0004	0.002	0.007	(Lab value)	68.6	2.50	15.9	2.34	182.5
1.0×10^{-18}	0.0004	0.002	0.007	(Small value)	70.6	2.57	16.3	2.40	185.1
1.0×10^{-17}	0.004	0.002	0.002	(Zero)	36.4	1.33	8.8	1.29	128.9
1.0×10^{-17}	0.004	0.002	0.002	(Lab value)	35.8	1.30	8.7	1.28	126.6
1.0×10^{-17}	0.004	0.002	0.002	(Small value)	36.4	1.33	8.8	1.29	128.1
1.0×10^{-18}	0.0004	0.018	0.06	(Zero)	71.9	2.62	16.6	2.44	102.4
6.0×10^{-19}	0.00024	0.008	0.06	(Zero)	86.8	3.16	19.8	2.91	150.3
6.0×10^{-19}	0.00024	0.008	0.06	(Small value)	88.8	3.23	20.2	2.97	151.8
5.0×10^{-16}	0.2	0.1	0.02	(Zero)	28.4	1.04	7.1	1.04	11.7
5.0×10^{-16}	0.2	0.1	0.02	(Lab value)	24.7	0.90	6.3	0.93	10.3
5.0×10^{-16}	0.2	0.1	0.02	(Small value)	28.1	1.02	7.0	1.03	11.6
1.0×10^{-18}	0.0004	0.06	0.21	(Zero)	67.5	2.46	15.8	2.32	34.6
1.0×10^{-18}	0.0004	0.06	0.21	(Small value)	61.7	2.25	14.3	2.10	33.4
5.0×10^{-19}	0.0002	0.08	0.4	(Zero)	81.5	2.97	18.7	2.75	26.8
5.0×10^{-19}	0.0002	0.08	0.4	(Small value)	71.6	2.61	16.5	2.43	26.4

Table 5. **Results of Model 4.** S_s^0 **is** 15.4 **and** R_i^0 **is** 0.35 **[yr].**

κ [m^2]	ϖ [m^2/s]	w [m]	$w/w_{\rm hy}$	ϵ	S_s	S_s/S_s^0	R_i [yr]	R_i/R_i^0	ΔT_{max} [K]
1.0×10^{-17}	0.004	0.002	0.007	(Zero)	16.8	1.09	0.38	1.09	15.6
1.0×10^{-17}	0.004	0.002	0.007	(Lab value)	15.1	0.99	0.35	1	13.9
1.0×10^{-17}	0.004	0.002	0.007	(Small value)	16.6	1.08	0.38	1.09	15.4
1.0×10^{-16}	0.04	0.002	0.002	(Zero)	15.8	1.02	0.36	1.03	14.7
1.0×10^{-16}	0.04	0.002	0.002	(Lab value)	15.3	0.99	0.35	1	14.2
1.0×10^{-16}	0.04	0.002	0.002	(Small value)	15.7	1.02	0.36	1.03	14.7
1.0×10^{-17}	0.004	0.018	0.06	(Zero)	16.7	1.09	0.38	1.09	3.6
1.0×10^{-17}	0.004	0.018	0.06	(Lab value)	6.9	0.45	0.23	0.66	1.3
1.0×10^{-17}	0.004	0.018	0.06	(Small value)	15.3	0.99	0.35	1	3.3
6.0×10^{-18}	0.0024	0.008	0.04	(Zero)	17.2	1.12	0.39	1.11	8.0
6.0×10^{-18}	0.0024	0.008	0.04	(Lab value)	10.1	0.66	0.26	0.74	4.3
6.0×10^{-18}	0.0024	0.008	0.04	(Small value)	16.3	1.06	0.37	1.06	7.5
5.0×10^{-15}	2	0.1	0.02	(Zero)	15.4	1.00	0.35	1	0.6
5.0×10^{-15}	2	0.1	0.02	(Lab value)	12.3	0.80	0.30	0.86	0.5
5.0×10^{-15}	2	0.1	0.02	(Small value)	15.1	0.98	0.35	1	0.6
1.0×10^{-17}	0.004	0.06	0.21	(Zero)	16.7	1.08	0.38	1.09	1.1
1.0×10^{-17}	0.004	0.06	0.21	(Lab value)	–	–	0.21	0.6	0.4
1.0×10^{-17}	0.004	0.06	0.21	(Small value)	12.4	0.80	0.30	0.86	0.8
5.0×10^{-18}	0.002	0.08	0.4	(Zero)	17.0	1.11	0.38	1.09	0.9
5.0×10^{-18}	0.002	0.08	0.4	(Lab value)	–	–	0.19	0.54	0.2
5.0×10^{-18}	0.002	0.08	0.4	(Small value)	9.8	0.63	0.25	0.71	0.5

Table 6. **Results of Model 5.** S_s^0 **is** 18.5 **and** R_i^0 **is** 0.77 **[yr].**

κ [m^2]	ϖ [m^2/s]	w [m]	$w/w_{\rm hy}$	ϵ	S_s	S_s/S_s^0	R_i [yr]	R_i/R_i^0	ΔT_{max} [K]
1.0×10^{-17}	0.004	0.002	0.007	(Zero)	23.0	1.24	0.95	1.23	49.5
1.0×10^{-17}	0.004	0.002	0.007	(Lab value)	20.9	1.13	0.86	1.12	44.9
1.0×10^{-17}	0.004	0.002	0.007	(Small value)	22.8	1.23	0.96	1.23	49.1
1.0×10^{-16}	0.04	0.002	0.002	(Zero)	19.8	1.07	0.82	1.06	43.7
1.0×10^{-16}	0.04	0.002	0.002	(Lab value)	19.2	1.04	0.8	1.04	42.4
1.0×10^{-16}	0.04	0.002	0.002	(Small value)	19.7	1.07	0.82	1.06	43.6
1.0×10^{-17}	0.004	0.018	0.06	(Zero)	23.0	1.24	0.95	1.23	10.7
1.0×10^{-17}	0.004	0.018	0.06	(Lab value)	9.2	0.50	0.43	0.56	4.5
1.0×10^{-17}	0.004	0.018	0.06	(Small value)	21.1	1.14	0.87	1.13	9.9
6.0×10^{-18}	0.0024	0.008	0.04	(Zero)	24.7	1.33	1.01	1.31	24.8
6.0×10^{-18}	0.0024	0.008	0.04	(Lab value)	14.3	0.77	0.61	0.79	15.0
6.0×10^{-18}	0.0024	0.008	0.04	(Small value)	23.5	1.27	0.97	1.26	23.8
5.0×10^{-15}	2	0.1	0.02	(Zero)	18.7	1.01	0.78	1.01	1.6
5.0×10^{-15}	2	0.1	0.02	(Lab value)	14.8	0.80	0.63	0.82	1.3
5.0×10^{-15}	2	0.1	0.02	(Small value)	18.3	0.99	0.76	0.99	1.6
1.0×10^{-17}	0.004	0.06	0.21	(Zero)	22.7	1.23	0.96	1.25	3.2
1.0×10^{-17}	0.004	0.06	0.21	(Lab value)	4.2	0.23	0.38	0.49	1.1
1.0×10^{-17}	0.004	0.06	0.21	(Small value)	16.7	0.90	0.70	0.91	2.4
5.0×10^{-18}	0.002	0.08	0.4	(Zero)	23.9	1.29	0.98	1.27	2.5
5.0×10^{-18}	0.002	0.08	0.4	(Small value)	13.4	0.73	0.58	0.75	1.5

Table 7. **Results of Model 4+.** S_s^0 **is** 15.4 **and** R_i^0 **is** 0.35 **[yr].**

κ [m^2]	ϖ [m^2/s]	w [m]	$w/w_{\rm hy}$	ϵ	S_s	S_s/S_s^0	R_i [yr]	R_i/R_i^0	ΔT_{max} [K]
1.0×10^{-17}	0.4	0.02	0.007	(Zero)	15.5	1.01	0.35	1.0	3.0
1.0×10^{-17}	0.4	0.02	0.007	(Lab value)	14.0	0.91	0.33	0.94	2.7
1.0×10^{-16}	4	0.02	0.002	(Zero)	15.4	1.00	0.35	1.0	3.0
1.0×10^{-16}	4	0.02	0.002	(Lab value)	14.9	0.97	0.34	0.97	2.9
1.0×10^{-17}	0.4	0.18	0.06	(Zero)	15.5	1.01	0.35	1.0	0.4
1.0×10^{-17}	0.4	0.18	0.06	(Lab value)	6.6	0.43	0.23	0.66	0.2
6.0×10^{-18}	0.24	0.08	0.04	(Zero)	15.5	1.01	0.36	1.03	0.8
6.0×10^{-18}	0.24	0.08	0.04	(Lab value)	9.2	0.60	0.25	0.71	0.5
5.0×10^{-15}	200	1	0.2	(Zero)	15.4	1.00	0.35	1.0	0.1
5.0×10^{-15}	200	1	0.2	(Lab value)	12.3	0.80	0.30	0.86	0.1
1.0×10^{-17}	0.4	0.6	0.21	(Zero)	16.7	1.08	0.38	1.09	0.1
1.0×10^{-17}	0.4	0.6	0.21	(Lab value)	–	–	0.21	0.6	0.06
5.0×10^{-18}	0.2	0.60	0.4	(Zero)	17.1	1.11	0.38	1.09	0.1
5.0×10^{-18}	0.2	0.8	0.4	(Lab value)	–	–	0.19	0.54	0.04